

Particulate samples on their filter substrates were directly mounted at the beamline for mapping by μ XRF and spectroscopy by extended μ XANES. Typically, a $500 \times 500\text{-}\mu\text{m}^2$ map was collected at 10 keV for each sample with an $\sim 5\text{-}\mu\text{m}$ step size, and $\sim 5\text{--}10$ Fe-rich spots of varying intensities were chosen randomly from the Fe $K\alpha$ map for spectroscopic analysis. Fe K-edge extended μ XANES spectra were collected between 7010 and 7415 eV, with 0.5-eV steps through the Fe K-edge region (7095–7140 eV), and at 1, 2 and 5-eV steps at higher energies. XANES spectra were corrected for detector dead-time, had their pre-edges subtracted, and normalised using software available at the beamline.^[15] Energy calibration was ensured using a reproducible glitch in the monochromator at 7263.64 eV and the spectra shifted as necessary.

Once a set of spectra such as those described above has been reduced to pre-edge-subtracted, post-edge-normalised form, the work of classification can begin. The first step is to do PCA on the set and decide how many components to retain. Separation of clusters may be possible with fewer components than is really necessary to describe the full variability of the dataset. Let the i th spectrum be denoted $y_i(E)$ with $i = 1 \dots n$. Using PCA, we approximate the set of spectra as:

$$y_i(E) \approx \sum_{\alpha=1}^M w_{i\alpha} \lambda_{\alpha} C_{\alpha}(E) \quad (1)$$

where M is the number of components retained, $w_{i\alpha}$ is the amount (loading) of component α assigned to spectrum i , λ_{α} is the eigenvalue (relative importance) of component α , and $C_{\alpha}(E)$ is the α th abstract component. The eigenvalues are sorted by magnitude so that the first component is the most important. The abstract components form an orthonormal set. For XANES data with a sufficiently long post-edge region, the first abstract component approximates the average of all the spectra, and the loadings of this component for all the individual spectra are all approximately the same. We can also perform the rotation given by iterative target factor analysis (ITFA^[16]), which seeks apparent end-members such that the loadings are all non-negative and as different from each other as possible, in which case we have

$$y_i(E) \approx \sum_{\alpha=1}^M X_{i\alpha} T_{\alpha}(E) \quad (2)$$

in which the loadings are $X_{i\alpha}$ and the components are $T_{\alpha}(E)$. If M is small enough, the ITFA components often look like identifiable XANES spectra.

If we simply make a scatterplot of, for instance, $w_{i2} \div w_{i1}$ v. $w_{i3} \div w_{i1}$, as is typically done with STXM (Scanning Transmission X-ray Microscope) stacks, we often find a poor separation between sets of points representing spectra from different types of materials. By a clever choice of coordinates, we can make these separations clear, essentially using the image-processing capabilities of the human visual system. The rotation we use is chosen from a restricted set that lets one look at combinations of four weights:

$$\begin{aligned} x_i &= w_{Ai} \cos \theta_1 + w_{\alpha i} \sin \theta_1 \\ y_i &= w_{Bi} \cos \theta_2 + w_{\beta i} \sin \theta_2 \end{aligned} \quad (3)$$

where axes A and B may be considered as ‘view’ axes, α and β are ‘hidden’ axes that are rotated into view and θ_1 and θ_2 are

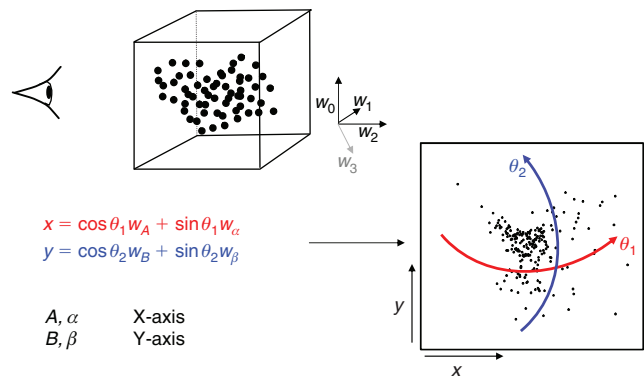


Fig. 2. Schematic of projection visualisation. In the upper half of the figure, we imagine viewing a two-dimensional projection of a higher-dimensional set of points with coordinate axes as shown. The bottom half shows the definition of the projection axes and suggests the visual effect of varying the two angles θ_1 , θ_2 .

rotation angles. A schematic of how the rotation works is shown in Fig. 2. In the visualisation program, which is written in LabVIEW, the rotation angles are controlled by sliders and the axes selected by switches. The projection is shown continuously as the parameters are changed, so that the user can select rotation axes and angles that produce interesting views. As one changes θ_1 , there is a strong visual impression of the cloud of points as a three-dimensional object rotating around a vertical axis. Similarly, changing θ_2 makes it appear as if the cloud of points is rolling around a horizontal axis. However, because the set of points exists in more than three dimensions, the choice of θ_1 affects the combination of loadings that are viewed as ‘into the screen’, hence the results of changing θ_2 .

When viewing abstract components, the weights used in Eqn 3 are not quite the outputs of PCA. As mentioned above, the loading of the first component is nearly constant and a measure of intensity in the spectrum. We therefore divide other component loadings by it. This normalisation is not done for ITFA components because there’s nothing special about the first one of these.

The tool has other useful features. It allows the user to select a point and see the corresponding spectrum, which is good for detecting outliers and verifying that points that are close together in projection really do correspond to similar-looking XANES spectra. It is possible to delineate clusters either by manual masking and selection or by k-means clustering.^[17] The memberships of clusters thus chosen may be recorded in text files, along with the parameters used in the projection.

Results

The tool described above was applied to the Western Subarctic Pacific group (Group 1), with results shown in Fig. 3. This is a stereogram obtained by taking two views with θ_1 10° apart, with the points coloured according to which group (in the projected 3-D space) they belong to. Outliers are in white. The projections were done using the first six abstract PCA components. We see four distinct clusters, coloured yellow, red, cyan and purple, suggesting four distinct types of material.

Next, we averaged the XANES spectra for each cluster, as shown in Fig. 4 and performed linear combination fitting with non-negative loadings to a large database of Fe references. This database is a revised and extended version of one used in a study of Fe XANES classification.^[18] Each cluster average fit to

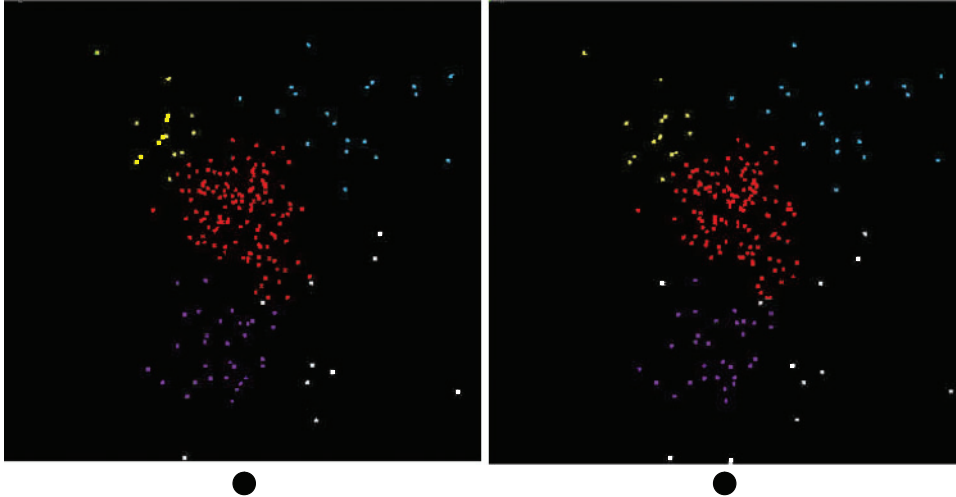


Fig. 3. Stereogram showing projections for Group 1 (Western Subarctic Pacific). The clusters are colour-coded red (0), yellow (1), cyan (2), purple (3) and white (outliers). The two views are taken with values of θ_1 differing by 10° . Clusters were defined by manual selection and masking.

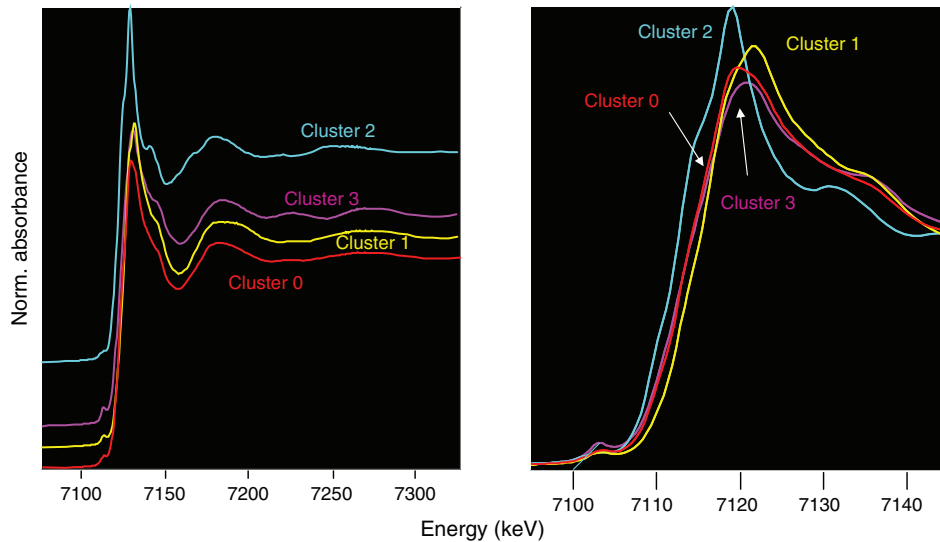


Fig. 4. Averaged X-ray absorption near-edge spectroscopy spectra for the clusters for Group 1 (Western Subarctic Pacific), shown in colours corresponding to Fig. 3. The right-hand graph is a zoom-in on the near edge energy region of the data on the left.

mixtures of 1–3 minerals, as identified in Table 1. As an aside, we note that the difference between the Cluster 0 and Cluster 3 averages are subtle in the near-edge region but become more prominent in the extended region, thus showing the value of taking extended-range data even for XANES analysis.

The fits shown here for the cluster averages do not necessarily apply to the individual members. Because the cluster does take up a finite area in projection, it's obvious that the individual spectra differ from each other. Individual fits of several member of Cluster 2, for instance, always show the presence of Fe^{2+} phyllosilicates and Fe^{3+} -bearing clays, but also up to 25% of various other species such as magnetite and ferrihydrite. Thus, the fits to the cluster averages represent a simplification of the true diversity. However, the fits represent species consistently found in cluster members.

We tested the partitioning of spectra into clusters to see if this clustering really reflects diversity in the spectra. Let

the normalised signal for the i th spectrum in the c th cluster be denoted $y_i^c(E)$ at energy point E . Define the cluster mean $y_{\text{mean}}^c(E) = \langle y_i^c(E) \rangle_i$ where $\langle \dots \rangle_i$ represents a mean over spectra. Now define the overall mean as $\bar{y}(E) = \langle y_{\text{mean}}^c(E) \rangle_c$. Finally, define a diversity measure

$$d = \sum_{c,E} (y_{\text{mean}}^c(E) - \bar{y}(E))^2 / \sum_{c,E} \bar{y}(E)^2 \quad (4)$$

which is, essentially, a normalised variance among the different clusters. Now, do this operation for the actual selected clusters and for ‘clusters’ made of randomly chosen spectra, such that each ‘cluster’ has the same number of spectra in it as the real ones. Spectra are chosen for ‘cluster’ membership without replacement. After 10^5 trials, not once did the diversity measure for the random cluster equal or exceed that for the real ones. This result suggests that the clustering organises the spectra, which

Table 1. Fit results for cluster averages in Group 1 (Western Subarctic Pacific), shown in Fig. 4, and Group 2 (Southern Ocean), shown in Fig. 5. Outliers ($n = 12$ for group 1; $n = 6$ for group 2) are not listed. Species are aggregated into chemically similar groups. Named minerals (superscripts) are ones that appeared in the fits as the sole entries in their class. The Fe^{2+} silicate group contains hornblende and augite. The Fe^{2+} phyllosilicate group contains biotite and chlorite. The Fe^{3+} clay group contains Imt-1, ISCZ-1, KGa-1b and NAU-1 (Clay Minerals Society designations). The Fe^{3+} oxyhydroxide group contains 2-line and 6-line ferrihydrite and disordered biogenic oxide. Other minerals were considered in the fits but the ones listed here are what appeared in the best fits. Sum-square error NSS is given by $\Sigma(y_i - y_i^{\text{fit}})^2 \div \Sigma y_i^2$ where y_i is the signal value at the i th point. The error bars, estimated by the difference in amounts of species in fits using alternative combinations of minerals, are $\sim 10\%$

Cluster	Number of spectra	Fe^{2+} phyllosilicate (%)	Fe^{2+} silicate (%)	Fe^{3+} oxyhydroxide (%)	Fe oxide (%)	Fe^{3+} clays (%)	NSS ($\times 10^{-5}$)
Group 1. Western Subarctic Pacific							
1/0 (red)	132	18		44		38	1.2
1/1 (yellow)	16	5				95	3.0
1/2 (cyan)	19	71				31	4.1
1/3 (purple)	31		27 ^A	27	54 ^B		2.0
Group 2. Southern Ocean							
2/0 (white)	42		26 ^C	74			6.3
2/1 (red)	55			27		74	2.0
2/2 (yellow)	21		13 ^A		57 ^D	29	4.9

^AAugite.

^BMagnetite.

^CHornblende.

^DHematite.

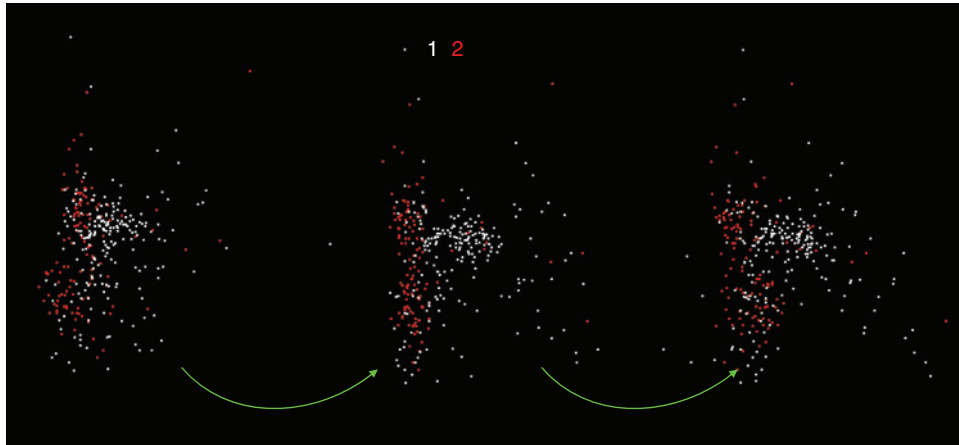


Fig. 5. Spectra of Group 2 (red, Southern Ocean) projected onto the space defined by the PCA of Group 1 (white, Western Subarctic Pacific). The three panels differ by increments of 10° in θ_1 , to give an impression of how the Southern Ocean cloud of points relates to the Western Subarctic Pacific points.

differ significantly from each other, into different groups, which random allocation would not do.

Now we can ask if the Southern Ocean group (Group 2) looks the same as the Western Subarctic Pacific. One way to do this is to project the data from the Southern Ocean group onto the same basis set as the Western Subarctic Pacific group, essentially fitting the Southern Ocean group to sums of the first few abstract components found in the Western Subarctic Pacific group. By doing so, we can plot the two groups together and see if the clouds of points occupy the same space. In Fig. 5, we show a set of three rotations in which Western Subarctic Pacific points are white and Southern Ocean points are red. The red points occupy a thin slab in the projected 3-D space, whereas the white points fill the space. This shows that the Southern Ocean differs from the Western Subarctic Pacific, but does not clearly show how. We then applied the visualisation tool to the Southern Ocean group independently from the Western Subarctic Pacific group and found that it generates three clusters plus 5% of outliers,

as shown in Fig. 6, in which the outliers are the blue points. These clusters were identified using k -means clustering^[17] rather than manual selection. Manual selection is an option because k -means doesn't always yield good separation. The averaged spectra from each of these clusters from the Southern Ocean are more similar to each other than those of the Western Subarctic Pacific group. One Southern Ocean cluster fits to a mix of Fe^{2+} silicates and Fe^{3+} -bearing oxyhydroxides. The second cluster fits to Fe^{3+} clays plus oxyhydroxides and has a spectrum quite similar to that of cluster 1 in the Western Subarctic Pacific (labelled in yellow), and the third fits to hematite and smaller amounts of Fe^{3+} clays and Fe^{2+} silicates (Table 1). The exact proportions depend on which species one takes in the fits. Two of the three clusters have averages that don't fit well to sums of the cluster averages from the Western Subarctic Pacific group, which shows again that the Southern Ocean group is outside the variability of the Western Subarctic Pacific group, except possibly for outliers.

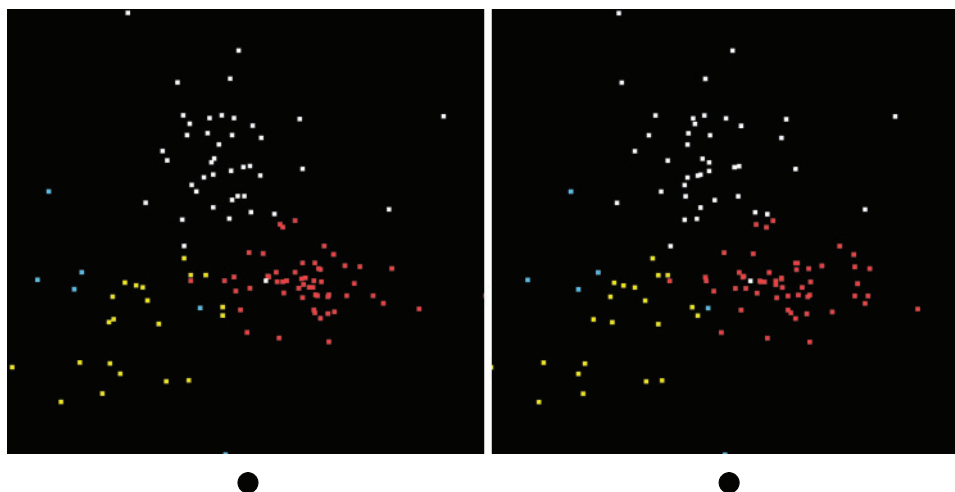


Fig. 6. Stereogram of Group 2 (Southern Ocean) spectra, analysed independently of Group 1 (Western Subarctic Pacific), showing clusters 0 (white), 1 (red) and 2 (yellow) as well as outliers (blue). Clusters were defined by k-means selection.

Discussion

As demonstrated above, the visualisation method is an effective way to identify clusters of similar data within a large and complex dataset so that the samples can be described in terms of a small number of types of material. Consideration of the linear combination fits of many tens to hundreds of individual spectra is an intractable problem because fits are not unique, and there is no easy way to get a sense of the overall variability in chemical speciation. The much-reduced set of variability that results from the visualisation method greatly facilitates comparisons between large datasets. In the examples presented here, the 209 spectra from the Western Subarctic Pacific were reduced to four main clusters (plus outliers), and the 126 spectra from the Southern Ocean were reduced to three main clusters (plus outliers).

Both regions contained significant amounts of Fe^{3+} oxyhydroxides and Fe^{3+} -containing clays (Table 1), pointing to the ubiquity of these Fe mineral groups in marine particulate iron regardless of ocean basin. In contrast, three of the four clusters in the Western Subarctic Pacific contained Fe^{2+} -containing phyllosilicates such as biotite or chlorite, and the fourth cluster contained significant magnetite. Neither of these mineral groups was present in the Southern Ocean clusters, indicating that these mineral groups are specific to the Western Subarctic Pacific and likely indicate the influence of the volcanic margin source of iron to that region.^[3,12] Likewise, hematite was found in the Southern Ocean samples but not in the Western Subarctic Pacific. Looking more closely at the Southern Ocean group samples, we find that certain species clusters are more prevalent at some stations than others (Fig. 7). Because hematite is a known, although minor, component of mineral dust,^[19] one might expect the hematite observed in our samples to derive from Australian dust. The observed higher relative abundance of the hematite-containing cluster 2 at the Polar Frontal Zone station P2 compared to the other, more northerly Subantarctic and Subtropical stations is at odds with the expected gradient from dust deposition, however, and suggests an as yet unidentified source of hematite to the Station P2 – Polar Front samples. Southern Ocean Cluster 1, which was composed entirely of Fe^{3+} clays and oxyhydroxides (Table 1), was the dominant species cluster at EAC-influenced subtropical stations 23 and 24. Of the three process stations, only station P3 (Subantarctic-east) was

strongly influenced by this species cluster (56% of spectra), suggesting that P3 may be the most influenced by EAC subtropical waters. Indeed, this is consistent with the conclusion derived from independent hydrographic and other trace metal data.^[14] These examples show the use of Fe mineralogy as determined by μXANES analysis in tagging the source of Fe to the ocean.

In the example above, we found that some clusters of Fe species dominated certain stations and not others. Furthermore, there was no clear trend in species clusters with depth in the water column, supporting the idea that lateral differences in Fe speciation are generally stronger than vertical ones.

All particulate iron bioavailability studies to date have been conducted on iron oxyhydroxides and iron oxides.^[20,21] This XANES analysis shows that iron oxyhydroxides and oxides are only part of the particulate iron in the ocean. Journet et al.^[22] and Schroth et al.^[23] have both shown that Fe-containing silicates (both clays and primary minerals) from putative atmospheric dust sources can have higher solubility than iron oxides. The abundance of clays and primary and secondary Fe-bearing silicates that we see in the water column begs for the examination of the bioavailability of these particulate iron species.

Although this work was done using spectra collected on selected points, the use of fast detectors on high-flux microprobes will make it possible to collect many more spectra without the need for manual selection of points. When thousands of spectra become available on each sample, some means of visualising the structure of the data will become even more important than it is now. The present work is a start towards developing such methods.

There are several possible extensions and modifications of the basic idea of projection and dimensional reduction. For instance, instead of using model-free PCA to provide coordinates, it may be possible and sensible in some cases to do least-squares fits with non-negative coefficients on each reference spectrum. In that case, it may be necessary to add together the weights of references that are ‘similar’.

There is a class of methods called projection pursuit,^[24] in which an automatic procedure is used to look for projections that are ‘interesting’ in some sense. For instance, a common criterion is that the distribution in projection should be as non-Gaussian as possible. Such an automated tool may be useful for finding

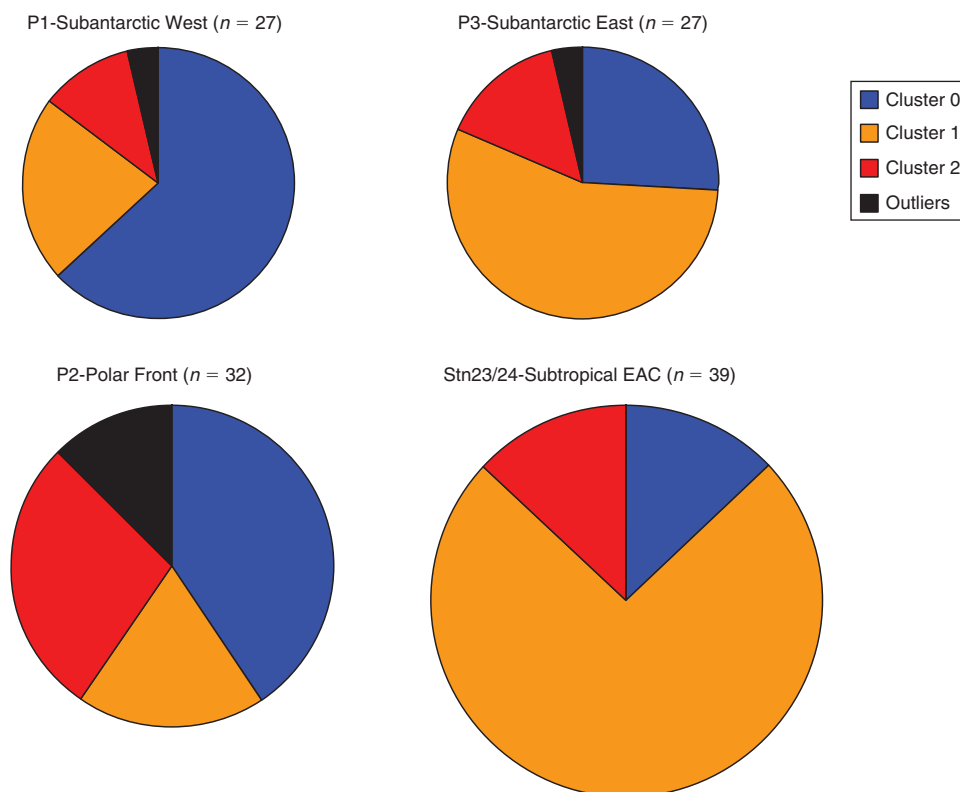


Fig. 7. Prevalence of cluster members at four locations in the Southern Ocean (Group 2). Cluster averages are as defined in Table 1 and are: cluster 0–26 % Fe^{2+} silicates, 74 % Fe^{3+} oxyhydroxides; cluster 1–27 % Fe^{3+} oxyhydroxides, 74 % Fe^{3+} clays; cluster 2–13 % Fe^{2+} silicates, 57 % hematite, 29 % Fe^{3+} clays. The areas of the pies are proportional to the number of spectra from each location, also indicated in parentheses.

combinations of coordinates not easily discovered by manual exploration.

Another class of methods starts by connecting together near-neighbour spectra into a graph (in the mathematical sense) and attempting to infer the underlying geometry of that graph. Here, ‘near-neighbour’ refers to distances between spectra computed as norms of differences between them. In spectral clustering,^[25] this graph is manipulated to label each spectrum with a set of coordinates in a lower-dimensional space, such as PCA does, but without the requirement of a linear mapping between spectra and this new space. Automatic clustering methods are then used for classification, which could, in principle, be augmented with a visualisation tool such as ours. In another approach, the network of connections between spectra is fitted to the geometry of an assumed lower-dimensional manifold so that the derived points on this manifold bear the same relationship to nearby points as the corresponding spectra do to their neighbours, for example by requiring that the shortest distance between any two spectra match the geodesic distances between the corresponding points in the manifold.^[26,27] Such sophisticated methods, perhaps combined with interactive visualisation tools, may be the way forward when the number of spectra goes into the hundreds or thousands.

We have demonstrated an approach to making the transition from acquiring spectra on inhomogeneous samples to acquiring a physical understanding of them. In the example shown here, we showed that data from hundreds of spectra could be simplified and some of the differences between iron-bearing particles from two parts of the ocean teased out. The combination of computation plus human visual evaluation results in a powerful tool for data analysis.

Supplementary material

An executable file of the classification program and a short ‘how-to’ guide to it are available for download from the journal, as is a copy of the Fe XANES database as used in this paper. This database does not include several species, such as Fe carbides, as they were not considered plausible possibilities for the present project.

Acknowledgements

The operations of the Advanced Light Source at Lawrence Berkeley National Laboratory are supported by the Director, Office of Science, Office of Basic Energy Sciences, US Department of Energy under contract number DE-AC02-05CH11231. Collection of samples for the VERTIGO project was supported by the US National Science Foundation Program in Chemical Oceanography to Ken Buesseler and the US Department of Energy, Office of Science, Biological and Environmental Research Program to Jim Bishop. The SAZ-SENSE project was supported by the Australian Government Cooperative Research Centres Programme. Collection of spectroscopic data by P.J.L. was supported through the WHOI Postdoctoral Scholar Program, WHOI Independent Study Award and NSF Chemical Oceanography. Thanks to S. Fakra, S. Bone and D. Ohnemus for assistance at the beamline. The authors thank Thomas Borch, Jakob Frommer and Andreas Voegelin for the use of several of their Fe reference spectra, as well as those sources acknowledged in Marcus et al.^[18]

References

- [1] A. Manceau, N. Tamura, M. A. Marcus, A. A. MacDowell, R. S. Celestre, R. E. Sublett, G. Sposito, H. A. Padmore, Deciphering Ni sequestration in soil ferromanganese nodules by combining X-ray fluorescence, absorption and diffraction at micrometer scales of resolution. *Am. Mineral.* **2002**, *87*, 1494.

- [2] A. Manceau, M. A. Marcus, N. Tamura, Quantitative speciation of heavy metals in soils and sediments by synchrotron X-ray techniques, in *Applications of Synchrotron Radiation in Low-Temperature Geochemistry and Environmental Science* (Eds P. A. Fenter, M. L. Rivers, N. C. Sturchio, S. R. Sutton) **2002**, pp. 341–428 (Mineralogical Society of America: Washington, DC).
- [3] P. J. Lam, D. C. Ohnemus, M. A. Marcus, The speciation of marine particulate iron adjacent to active and passive continental margins. *Geochim. Cosmochim. Acta* **2012**, *80*, 108. doi:10.1016/J.GCA.2011.11.044
- [4] I. J. Pickering, L. Gumaelius, H. H. Harris, R. C. Prince, G. Hirsch, J. A. Banks, D. E. Salt, G. N. George, Localizing the biochemical transformations of arsenate in a hyperaccumulating fern. *Environ. Sci. Technol.* **2006**, *40*, 5010. doi:10.1021/ES052559A
- [5] M. A. Marcus, X-Ray photon-in/photon-out methods for chemical imaging. *Trends Analyt. Chem.* **2010**, *29*, 508. doi:10.1016/J.TRAC.2010.02.013
- [6] B. Etschmann, C. G. Ryan, J. Brugger, R. Kirkham, R. Hough, G. Moorhead, D. Siddons, G. De Geronimo, A. Kuczewski, P. Dunn, Reduced As components in highly oxidized environments: evidence from full spectral XANES imaging using the MAIA massively parallel detector. *Am. Mineral.* **2010**, *95*, 884. doi:10.2138/AM.2010.3469
- [7] J. Lawrence, G. Swerhone, G. Leppard, T. Araki, X. Zhang, M. West, A. Hitchcock, Scanning transmission X-ray, laser scanning, and transmission electron microscopy mapping of the exopolymeric matrix of microbial biofilms. *Appl. Environ. Microbiol.* **2003**, *69*, 5543. doi:10.1128/AEM.69.9.5543-5554.2003
- [8] B. P. von der Heyden, A. N. Roychoudhury, T. N. Mtshali, T. Tyliczszak, S. C. B. Myneni, Chemically and geographically distinct solid-phase iron pools in the Southern Ocean. *Science* **2012**, *338*, 1199. doi:10.1126/SCIENCE.1227504
- [9] M. Lerotic, C. Jacobsen, T. Schäfer, S. Vogt, Cluster analysis of soft X-ray spectromicroscopy data. *Ultramicroscopy* **2004**, *100*, 35. doi:10.1016/J.ULTRAMIC.2004.01.008
- [10] K. O. Buesseler, T. W. Trull, D. K. Steinberg, M. W. Silver, D. A. Siegel, S. Saitoh, C. H. Lamborg, P. J. Lam, D. M. Karl, N. Z. Jiao, M. C. Honda, M. Elskens, F. Dehairs, S. L. Brown, P. W. Boyd, J. K. B. Bishop, R. R. Bidigare, VERTIGO (vertical transport in the global ocean): a study of particle sources and flux attenuation in the North Pacific. *Deep Sea Res. Part II Top. Stud. Oceanogr.* **2008**, *55*, 1522. doi:10.1016/J.DSR2.2008.04.024
- [11] J. K. B. Bishop, T. J. Wood, Particulate matter chemistry and dynamics in the twilight zone at VERTIGO ALOHA and K2 sites. *Deep Sea Res. Part I Oceanogr. Res. Pap.* **2008**, *55*, 1684. doi:10.1016/J.DSR.2008.07.012
- [12] P. J. Lam, J. K. B. Bishop, The continental margin is a key source of iron to the HNLC North Pacific ocean. *Geophys. Res. Lett.* **2008**, *35*, L07608. doi:10.1029/2008GL033294
- [13] C. H. Lamborg, K. O. Buesseler, P. J. Lam, Sinking fluxes of minor and trace elements in the North Pacific ocean measured during the VERTIGO program. *Deep Sea Res. Part II Top. Stud. Oceanogr.* **2008**, *55*, 1564. doi:10.1016/J.DSR2.2008.04.012
- [14] A. R. Bowie, D. Lannuzel, T. A. Remenyi, T. Wagener, P. J. Lam, P. W. Boyd, C. Guieu, A. T. Townsend, T. W. Trull, Biogeochemical iron budgets of the Southern Ocean south of Australia: decoupling of iron and nutrient cycles in the subantarctic zone by the summertime supply. *Global Biogeochem. Cycles* **2009**, *23*, GB4034. doi:10.1029/2009GB003500
- [15] M. A. Marcus, A. A. MacDowell, R. Celestre, A. Manceau, T. Miller, H. A. Padmore, R. E. Sublett, Beamline 10.3.2 at ALS: a hard X-ray microprobe for environmental and materials sciences. *J. Synchrotron Radiat.* **2004**, *11*, 239. doi:10.1107/S0909049504005837
- [16] A. Roßberg, T. Reich, G. Bernhard, Complexation of uranium(VI) with protocatechuic acid – application of iterative transformation factor analysis to EXAFS spectroscopy. *Anal. Bioanal. Chem.* **2003**, *376*, 631. doi:10.1007/S00216-003-1963-5
- [17] J. MacQueen (Ed.) Some methods for classification and analysis of multivariate observations, in *Proceedings of the fifth Berkeley Symposium on Mathematical Statistics and Probability, 21 June–18 July 1965, Berkeley, CA 1967*, pp. 281–297 (UC Berkeley Press: Berkeley, CA; and Cambridge University Press: London).
- [18] M. A. Marcus, A. J. Westphal, S. C. Fakra, Classification of Fe-bearing species from k-edge XANES data using two-parameter correlation plots. *J. Synchrotron Radiat.* **2008**, *15*, 463. doi:10.1107/S0909049508018293
- [19] C. D. Koven, I. Fung, Identifying global dust source areas using high-resolution land surface form. *J. Geophys. Res. – Atmos.* **2008**, *113*, D22204. doi:10.1029/2008JD010195
- [20] M. L. Wells, L. M. Mayer, R. R. L. Guillard, A chemical method for estimating the availability of iron to phytoplankton in seawater. *Mar. Chem.* **1991**, *33*, 23. doi:10.1016/0304-4203(91)90055-2
- [21] H. W. Rich, F. M. M. Morel, Availability of well-defined iron colloids to the marine diatom *Thalassiosira weissflogii*. *Limnol. Oceanogr.* **1990**, *35*, 652. doi:10.4319/LO.1990.35.3.0652
- [22] E. Journet, K. V. Desboeufs, S. Caquineau, J. L. Colin, Mineralogy as a critical factor of dust iron solubility. *Geophys. Res. Lett.* **2008**, *35*, L07805. doi:10.1029/2007GL031589
- [23] A. W. Schroth, J. Crusius, E. R. Sholkovitz, B. C. Bostick, Iron solubility driven by speciation in dust sources to the ocean. *Nat. Geosci.* **2009**, *2*, 337. doi:10.1038/NGEO501
- [24] P. J. Huber, Projection pursuit. *Ann. Stat.* **1985**, *13*, 435. doi:10.1214/AOS/1176349519
- [25] C. H. Yoon, P. Schwander, C. Abergel, I. Andersson, J. Andreasson, A. Aquila, S. Bajt, M. Barthelmess, A. Barty, M. J. Bogan, Unsupervised classification of single-particle X-ray diffraction snapshots by spectral clustering. *Opt. Express* **2011**, *19*, 16542. doi:10.1364/OE.19.016542
- [26] J. B. Tenenbaum, V. De Silva, J. C. Langford, A global geometric framework for nonlinear dimensionality reduction. *Science* **2000**, *290*, 2319. doi:10.1126/SCIENCE.290.5500.2319
- [27] S. T. Roweis, L. K. Saul, Nonlinear dimensionality reduction by locally linear embedding. *Science* **2000**, *290*, 2323. doi:10.1126/SCIENCE.290.5500.2323